propagating link sausage. Martin, Simmons, and Wunsch (1972) have demonstrated a variety of resonant triads for a constant-N stratification.

Among the infinity of possible resonant interactions, McComas and Bretherton (1977) have been able to identify three distinct classes that dominate the computed energy transfer under typical ocean conditions. Figure 9.15 shows the interacting propagation vectors in (k, m)-space. The associated frequencies ω are uniquely determined by the tilt of the vectors, in accordance with (9.4). Inertial frequencies (between f and $2f$, say) correspond to very steep vectors, buoyancy frequencies (between $\frac{1}{2}N$ and N) to flat vectors, as shown.

Elastic scattering tends to equalize upward and downward energy fluxes for all but inertial frequencies. Suppose that $\mathbf{k}_3$ is associated with waves generated near the sea surface propagating energy downward (at right angles to $\mathbf{k}_3$, as in figure 9.7). These are scattered into $\mathbf{k}_1$, with the property $m_1 = -m_3$, until the upward energy flux associated with $\mathbf{k}_1$ balances the downward flux by $\mathbf{k}_3$. The interaction involves a near-intertial wave $\mathbf{k}_2$ with the property $m_2 \approx 2m_3$. (The reader will be reminded of Bragg scattering from waves having half the wavelength of the incident and back-scattered radiation.) Similarly, for bottom-generated $\mathbf{k}_1$ waves with upward energy fluxes, elastic scattering will transfer energy into $\mathbf{k}_3$ waves.

Induced diffusion tends to fill in any sharp cutoffs at high wavenumber. The interaction is between two neighboring wave vectors of high wavenumber and frequency, $\mathbf{k}_1$ and $\mathbf{k}_3$, and a low-frequency low-wavenumber vector $\mathbf{k}_2$. Suppose the $\mathbf{k}_2$ waves are highly energetic, and that the wave spectrum drops sharply for wavenumbers just exceeding $|\mathbf{k}_3|$, such as $|\mathbf{k}_1|$. This interaction leads to a diffusion of action (energy/ω) into the low region beyond $|\mathbf{k}_3|$, thus causing $\mathbf{k}_1$ to grow at the expense of $\mathbf{k}_2$.

Parametric subharmonic instability transfers energy from low wavenumbers $\mathbf{k}_2$ to high wavenumbers $\mathbf{k}_1$ of half the frequency, $\omega_1 = \frac{1}{2}\omega_2$, ultimately pushing energy into the inertial band at high vertical wavenumber. The interaction involves two waves $\mathbf{k}_1$ and $\mathbf{k}_3$ of nearly opposite wavenumbers and nearly equal frequencies. The periodic tilting of the isopycnals by $\mathbf{k}_2$ varies the buoyancy frequency at twice the frequency of $\mathbf{k}_1$ and $\mathbf{k}_3$. (The reader will be reminded of the response of a pendulum whose support is vertically oscillated at twice the natural frequency.)

The relaxation (or interaction) time is the ratio of the energy density at a particular wavenumber to the net energy flux to (or from) this wavenumber. The result depends, therefore, on the assumed spectrum. For representative ocean conditions, McComas (in preparation) finds the relaxation time for elastic scattering to be extremely short, of the order of a period, and so up- and downgoing energy flux should be in balance. This result does not apply to inertial frequencies, consistent with observations by Leaman and Sanford (1975) of a downward flux at these frequencies. The relaxation time for induced diffusion is typically a fraction of a period! (This is beyond the assumption of the perturbation treatment.) Any spectral bump is quickly wiped out. The conclusion is that the resonant interactions impose strong restraints on the possible shapes of stable spectra.

In a challenging paper, Cox and Johnson (1979) have drawn a distinction between radiative and diffusive transports of internal wave energy. In the examples cited so far, energy in wave packets is radiated at group velocity in the direction of the group velocity. But suppose that wave-wave interactions randomize the direction of the group velocity. Then eventually the wave energy is spread by diffusion rather than radiation. The relevant diffusivity is $\kappa = \frac{1}{3}\langle c_g^2 \rangle \tau$, where τ is the relaxation time of the nonlinear interactions. Cox and Johnson have estimated energy diffusivities and momentum diffusivities (viscosities); they find that beyond 100 km from a source, diffusive spreading is apt to dominate over radiative spreading. There is an interesting analogy to crystals, where it is known that energy associated with thermal agitation is spread by diffusion rather than by radiation. The explanation lies in the anharmonic restoring forces between molecules, which bring about wave-wave scattering at room temperatures with relaxation times in the nanoseconds.

9.7 Breaking

This is the most important and least understood aspect of our survey. Longuet-Higgins has mounted a broadly based fundamental attack on the dynamics of breaking surface waves, starting with Longuet-Higgins and Fox (1977), and this will yield some insight into the internal-wave problems. At the present time we depend on laboratory experiments with the interpretation of the results sometimes aided by theoretical considerations.

Figure 9.16 is a cartoon of the various stages in an experiment performed by Thorpe (1978b). A density transition layer is established in a long rectangular tube. An internal wave maker generates waves of the first vertical mode. Before the waves have reached the far end of the tube, the tube is tilted through a small angle to induce a slowly accelerating shear flow. The underlying profiles of density, shear, and vertical displacement correspond roughly to the situation in figure 9.13.

For relatively steep waves in a weak positive[8] shear, the waves have sharpened crests. At the position of the crest, the density profile has been translated upward and steepened (B_1). There is significant wave energy loss in this development (Thorpe, 1978c, figure 10).

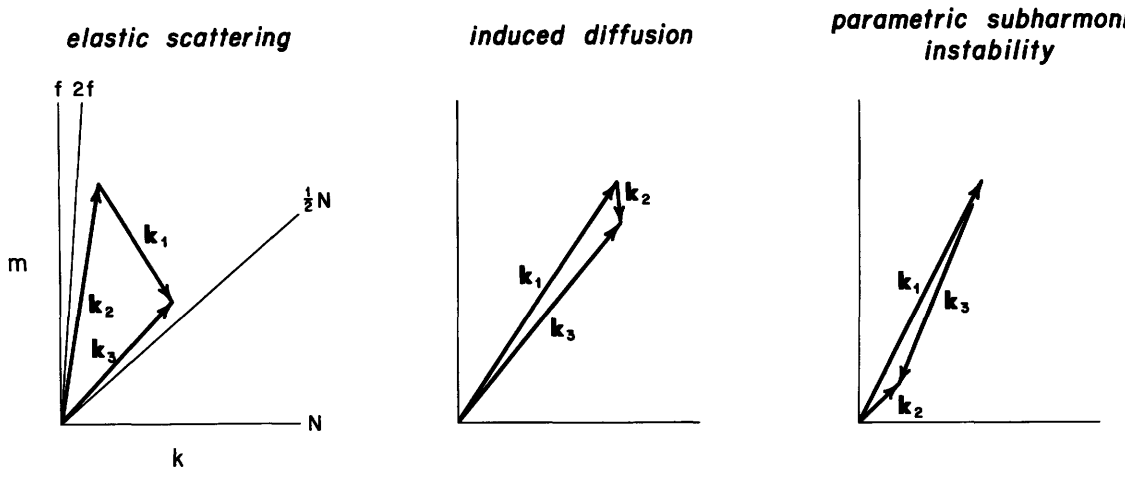

Figure 9.15 Resonant triads for three limiting classes of interaction, according to McComas and Bretherton (1977). The propagation vectors are drawn in (k, m)-space. Radial lines designate the tilt of the **k** vectors for $\omega = f, 2f, \frac{1}{2}N, n$. taking $N = 24f$.

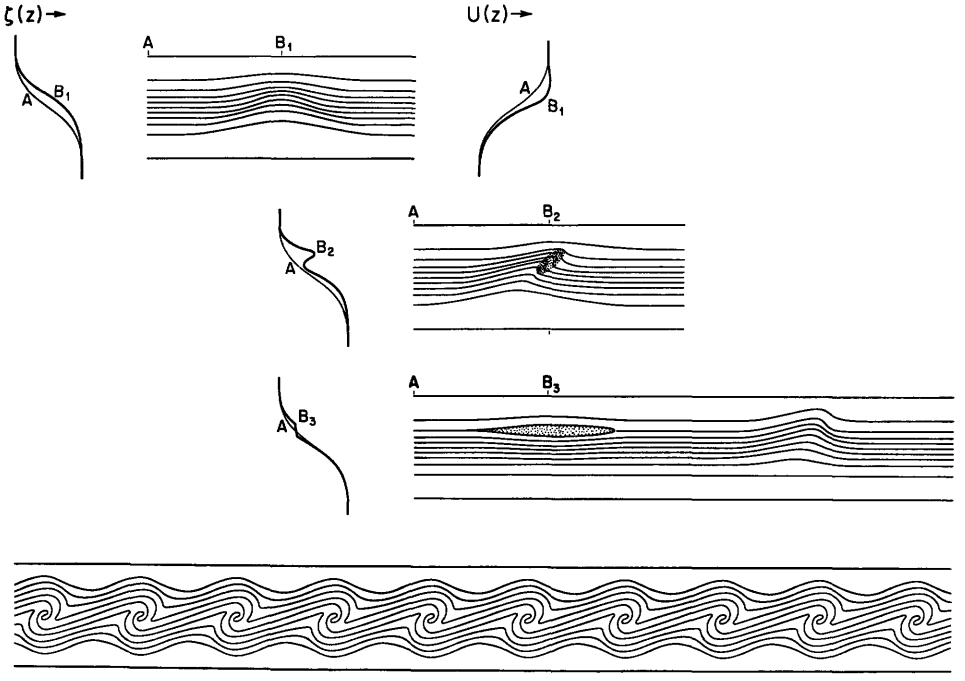

Figure 9.16 Cartoon for various stages of Thorpe's experiment. The early stages lead to the development of *advective* instability (upper three sketches), and the final stage to *shear* instability (bottom). Waves are traveling from left to right; the mean flow is forward (in the direction of wave propagation) above the density transition layer and backward below the transition layer. The density profiles along the indicated vertical sections are shown to the left; a velocity profile is shown to the top right (thin lines give the undisturbed profiles).

With increased positive shear, or with increased time, the particles at the crest accelerate, the isopycnal wave front becomes momentarily vertical, and a jet of fluid moves forward of the crest (B_2). The resulting density inversion gives rise to a Rayleigh-Taylor instability, forming a turbulent patch (shaded) whose turbulent energy is irretrievably lost to the organized wave motion. The turbulent patch becomes fairly well mixed, and introduces a steplike feature into the density profile (B_3). The patch spreads horizontally under the influence of the ambient stratification, forming *blini*, or pancakes. The detailed dynamics are complicated (Barenblatt and Monin, 1979); it is possible that in the oceans the spreading of the patches is eventually retarded by geostrophic confinement.

In Thorpe's laboratory experiment, the later stages of horizontal spreading are interrupted by the sudden formation of billows that grow rapidly, extracting energy from the mean shear flow (bottom of figure). Their wave length is quite short, only several times the thickness of the transition layer.

Hence, Thorpe (1978b, 1979) distinguishes between two types of instability leading to internal wave breaking. In the case of *advective instability*, breaking grows out of existing large-amplitude internal waves: more precisely, waves associated with steep isopycnal slopes. Eventually the particles in the crest are advected forward of the crest, leading to a local density inversion with the potential for a Rayleigh-Taylor instability. Advective instability can take place in the absence of ambient shear, though it is advanced by shear. The second type is induced *shear instability* (Kelvin-Helmholtz instability in the limit of an abrupt density transition), and can take place even in the absence of any (finite) wave disturbance, but is catalyzed by an existing wave background.

The two types appear as end points on a stability curve in slope-shear space, constructed by Thorpe (1978b, 1979) from theory and experiment (figure 9.17). Under the conditions described by the author, internal waves on a transition layer are unstable if their slope exceeds 0.34 in the absence of ambient shear, and if the shear exceeds $2N$ in the absence of slope. Away from the end points, there is advective instability modified by shear, and shear (K-H) instability modified by advection. The stability curve for the transition profile is not symmetric, implying that (under the prescribed geometry) negative shear delays instability.

The essential feature of advective instability is that the particle speed at the crest eventually exceeds the wave speed. The stability curve in figure 9.16 has been constructed from $u_{crest} = c$ (carrying the theory to third order in wave slope). This is in fair agreement with experiment. From a similar point of view, Orlanski and Bryan (1969) had previously derived the required critical amplitude for advective instability in the oceans, and have checked their analysis with numerical experiments. They conclude that more than enough internal wave energy exists for this type of instability to occur. They also conclude that conditions favor advective instability over shear instability, by the following very simple argument. From (9.12),

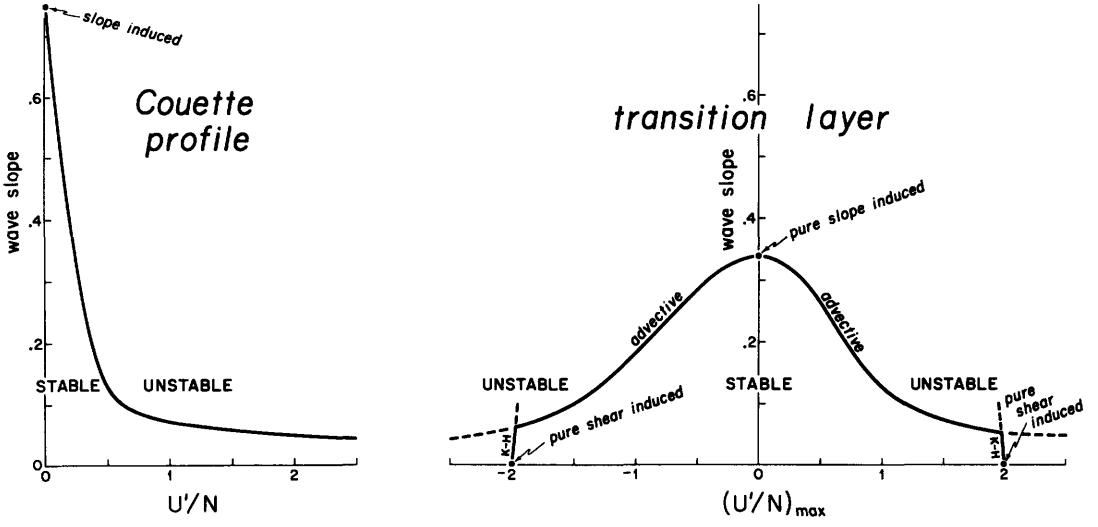

Figure 9.17 Stability diagram for internal waves in a shear flow for a Couette profile (as in figure 9.12) and for a transition layer (as in figure 9.13). Slope is defined as π·wave height/wavelength. The ordinate is U'/N (or $\pm Ri^{-1/2}$), with U in the direction of wave propagation. For the transition profile, U' and N^2 are proportional to $\mathrm{sech}^2(z - h)$, and hence $U'/N \sim \mathrm{sech}(z - h)$ has its maximum value at the transition $z = h$. The curves are drawn for the specific dimensions described by Thorpe (1978a, 1979).

$$\frac{mu}{N} = \frac{u}{\omega/k}\left(\frac{1-\omega^2/N^2}{1-f^2/\omega^2}\right)^{1/2}$$

$$\approx \frac{u}{\omega/k} \qquad \text{for} \quad f \ll \omega \ll N. \tag{9.16}$$

But $mu/N = Ri^{-1/2} = 2$ for shear instability, and $u/(\omega/k) = 1$ for advective instability. The linearized[9] treatment then says that waves have to be twice as high to be shear unstable than to be advectively unstable. The trouble with this argument is that it is limited to the self-shear of an elementary wave train, and does not take into account the imposed ambient shear (possibly due to other components of the internal wave spectrum). Thorpe's stability plot (figure 9.17) shows that the instabilities can go either way, depending on wave slope and the ambient shear.

McEwan (1973) has generated breaking internal waves in the laboratory by crossing two internal wave beams from separate sources. He finds that the breaking is associated with localized, abruptly appearing intensification in density gradient and shear. These "traumata" persist and spread, and become the locus of incipient turbulence. True turbulent disorder was always preceded by the sudden and widespread occurrence of the traumata.

In some further laboratory experiments with breaking internal waves, McEwan (personal communication) has estimated separately the work done in generating internal waves (allowing for wall friction), and the fraction of this work going into mixing, e.g., going into the increase in the potential energy of the mean stratification. The remaining energy is dissipated into heat. McEwan finds that something less than $\frac{1}{4}$ of the input energy goes into mixing, in support of an estimate by Thorpe (1973b). (In the ocean, the mixing of salt and heat may proceed at different rates because of the disparity in the diffusivities.) Thompson (1980) argues that this ratio is, in fact, the critical Richardson number.

All of this points toward a strong connection between breaking internal waves and the microstructure of density and velocity. Evidently, breaking internal waves can modify a density profile, reducing gradients in turbulent patches and sharpening them elsewhere. This can lead to a steppy fine structure. But we have shown that internal wave shear is concentrated at the steps, thus producing conditions for shear instability, and renewed breaking. This is like the chicken and the egg: which comes first?

9.8 Ocean Fine Structure and Microstructure

Measurements by Gregg (1975) off Cabo San Lucas and in the North Pacific gyre (figure 9.18 and table 9.1) speak for great geographic variability in the mixing processes. (This is apart from the *local* patchiness in microstructure even in regions of strong mixing.) Three water masses intermingle off Cabo San Lucas: the saline outflow from the Gulf of California, the relatively fresh waters being brought in from the northwest by the California Current, and Equatorial Water of intermediate salinity from the eastern tropical Pacific. MR6 remains in Equatorial Water. MR7 is from a shallower drop taken the next day within a few kilometers of MR6. Here we see the intermingling of the three water masses, each jostling for a level appropriate to its density.

Temperature inversions (negative dT/dz) are generally balanced by positive salinity gradients, so that the density increases with depth, and N^2 is positive. The temperature inversions have typical vertical scales of 5 m, with a step structure (e.g., just beneath feature D) attributed to the *diffusive* regime of double diffusion. The underside of temperature inversions (just above E) is often characterized by strong salinity inversions (positive dS/dz), and by prominent microstructure attributed to the *fingering* regime of double diffusion. Double-diffusive processes can be very important locally; they are discussed by J. S. Turner in Chapter 8.

Occasional density inversions (such as at 13 m depth in MR7) are accompanied by intense microstructure. These inversions are very local, and they disappear in a plot of 3-m averages. We are tempted to attribute the density inversions and associated intermittent microstructure to internal wave breaking.

MR7 is a good example of *intrusive* fine structure. Stommel and Fedorov (1967) gave the first discussion of such features based on their measurements near Timor and Mindanao. At the bottom of a well-mixed layer they found a pronounced temperature inversion (balanced by high salinity) that could be traced for 200 km! Evidently the warm saline water was formed 1 or 2 months earlier over the Australian continental shelf at a distance of 500 km, sliding down along an isopycnal surface. The thickness of the inversion layer varied from 20 to 40 m. Beneath the inversion layer, a number of warm, saline lamina of typically 5-m thickness could be traced over 5 km. All these features are associated with horizontal pressure gradients that must be geostrophically balanced. The authors made some calculations of the rate of lamina spreading associated with frictional dissipation in Ekman spirals above and beneath the lamina boundaries. Once the lamina are thinner than 1 m, they are swiftly conducted away. I refer the reader to Stommel and Fedorov's stimulating discussion.

Table 9.1 summarizes some statistical parameters. For comparison we have included MSR4 from the mid-gyre of the central North Pacific (Gregg, Cox, and Hacker, 1973). The three stations MR7, MR6, and MSR4 characterize strongly intrusive, weakly intrusive

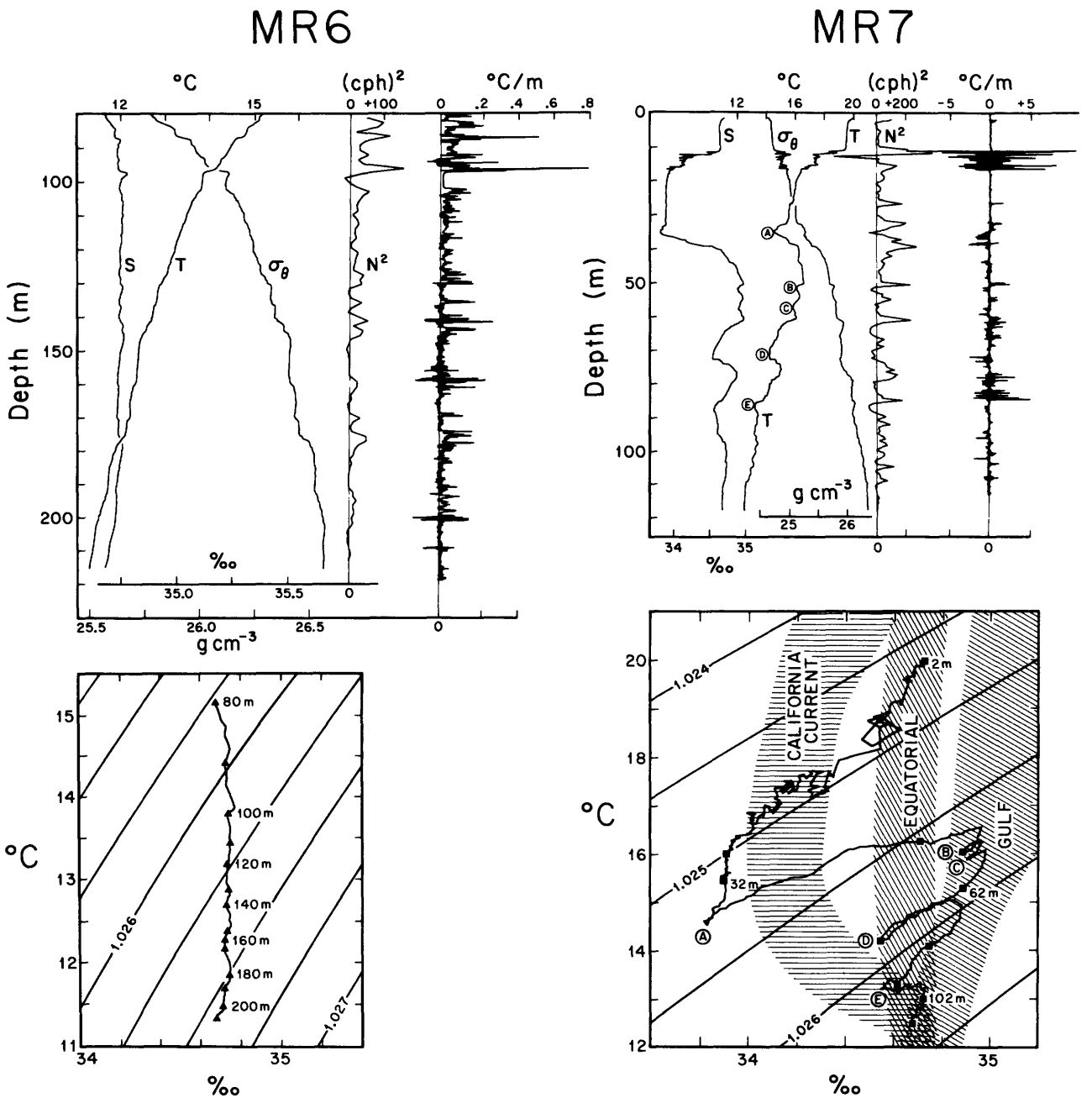

Figure 9.18 The water structure at two stations 60 km south-west of Cabo San Lucas (the southern tip of Baja California), and the associated T-S diagrams (from Gregg, 1975). The measurements have been processed to give the fine structure of S, T, σ_θ, N and the microstructure of dT/dz. Note differences in scale. The *cuspy* T-S diagram for MR7 is an indication of intrusive fine structure.

Table 9.1 Variances and Spectra of Vertical Gradients in the Ocean Fine Structure and Microstructure at Two Stations off Cabo San Lucas (MR7 and MR6) and in the Mid-Gyre of the Central North Pacific (MSR4)

	MR7			MR6			MSR4[a]		
	Strongly intrusive						Nonintrusive		
$\langle\lvert\partial_z T - \partial_z \bar{T}\rvert^2\rangle$ in $\left(\frac{°C}{m}\right)^2$		26			9×10^{-3}			1×10^{-3}	
$\langle\partial_z T\rangle^2$ in $\left(\frac{°C}{m}\right)^2$		4×10^{-3}			8×10^{-4}			6×10^{-4}	
Thermal diffusivity in $cm^2\,s^{-1}$		8[b]			0.015			0.002	
Cycles per meter	0.1	1	10	0.1	1	10	0.1	1	10
Spectrum of									
$\partial_z T$ in $\left(\frac{°C}{m}\right)^2/\text{cpm}$	2×10^{-1}	1×10^{-2}	1×10^{-2}	2×10^{-3}	2×10^{-4}	7×10^{-5}	7×10^{-4}	1×10^{-4}	3×10^{-5}
$\partial_z S$ in $\left(\frac{‰}{m}\right)^2/\text{cpm}$	2×10^{-2}	1×10^{-3}	8×10^{-4}	5×10^{-5}	1×10^{-5}	?	4×10^{-6}	8×10^{-6}	2×10^{-5}
$\partial_z \rho$ in $\left(\frac{g\,cm^{-3}}{m}\right)^2/\text{cpm}$	2×10^{-9}	7×10^{-10}	7×10^{-10}	2×10^{-10}	2×10^{-11}	?	2×10^{-11}	1×10^{-11}	9×10^{-12}
Spectrum of									
$a\,\partial_z T$ in $\left(\frac{g\,cm^{-3}}{m}\right)^2/\text{cpm}$	2×10^{-8}	1×10^{-9}	1×10^{-9}	2×10^{-10}	2×10^{-11}	?	3×10^{-11}	4×10^{-12}	1×10^{-12}
$b\,\partial_z S$ in $\left(\frac{g\,cm^{-3}}{m}\right)^2/\text{cpm}$	1×10^{-8}	0.6×10^{-9}	0.5×10^{-9}	0.3×10^{-10}	0.6×10^{-11}	?	0.3×10^{-11}	5×10^{-12}	13×10^{-12}
$\partial_z \rho$ in $\left(\frac{g\,cm^{-3}}{m}\right)^2/\text{cpm}$	0.2×10^{-8}	0.7×10^{-9}	0.7×10^{-9}	2×10^{-10}	2×10^{-11}	?	2×10^{-11}	10×10^{-12}	9×10^{-12}

a. MSR4 is not necessarily representative for the mid-gyre; subsequent cruises have given larger mean-square gradients.
b. The vertical heat flux for MR7 can probably not be modeled by an eddy coefficient (Gregg, 1975).

and nonintrusive situations, respectively. The conclusions are: (1) The ratio of the mean-square gradient to the mean gradient squared (the "Cox number") for temperature is highly variable, from 5000 at MR7 to 2 in the mid-gyre. Under certain assumptions (Osborn and Cox, 1972), the eddy diffusivity is the molecular diffusivity times this ratio, giving values all the way from 8 to 0.002 $cm^2\,s^{-1}$ (but see the footnote to table 9.1). The canonical value of 1 $cm^2\,s^{-1}$ [for which I am partly responsible (Munk, 1966)] is of no use locally. (2) Spectral levels in vertical gradients diminish with increasing vertical wavenumber up to 1 cpm, and then level off. (3) The relative contributions to the density-gradient spectrum has been estimated from $\partial_z \rho = -a\,\partial_z T + b\,\partial_z S$, with $a = 1.7 \times 10^{-4}\,g\,cm^{-3}(°C)^{-1}$, $b = 8 \times 10^{-4}\,g\,cm^{-3}(‰)^{-1}$. For MR7 at 0.1 cpm, the measured density gradient is much smaller than that inferred from either temperature alone or salinity alone. This is consistent with the near cancellation between temperature and salinity for intrusive features. (4) At higher wavenumbers for MR7, and at all wavenumbers of MR6 and MSR4, the density gradient spectrum is of the same order as that inferred from temperature or salinity alone, thus implying the dominance of internal waves.

Probability densities of the temperature gradients are highly non-Gaussian with an enormous flatness factor (138 for MR7, 55 for MR6) attesting to the patchiness (Gregg, 1975). The construction of meaningful ensemble averages in a highly intermittent environment (space and time) is an important task for the future.

To return now to internal waves, we can distinguish between two quite different effects on vertical profiles: (1) an (irreversible) microstructure and fine structure associated with intermittent internal wave breaking, and (2) a (reversible) fine structure due to the vertical straining of an otherwise smooth profile by internal waves of short vertical wavelength. The reversible contribution to fine structure by internal waves was first noticed by Lazier (1973b) and Garrett (1973). How are we to distinguish it from diffusive (and other irreversible) fine structure?

Let δT and δS designate departures in (potential) temperature and salinity from some long-time or long-distance averages $T_0(z)$, $S_0(z)$ at the same depth. Then

$$\delta\rho = -a\,\delta T + b\,\delta S$$

is the associated density departure, with $a(T, S, p)$ and $b(T, S, p)$ designating the (positive) coefficients of ther-

mal expansion and haline contraction. Take first the case of an intrusion only (figure 9.19). If it is totally compensated,

$$\delta\rho = 0,$$

and if it is not totally compensated, it soon will be (in a time of order N^{-1}). It follows that any vertical displacement of the isopycnals is not intrusive but due to a vertical displacement of the water, which we associate with internal waves (see next section). The vertical displacement ζ can be found from conservation of potential density:

$$\rho(z + \zeta) = \rho_0(z).$$

For the case of internal waves only, conservation of potential temperature and salinity give

$$T(z + \zeta) = T_0(z), \qquad S(z + \zeta) = S_0(z),$$

and the ζ-values from the three preceding equations should be the same:

$$\zeta_\rho = \zeta_T = \zeta_S. \tag{9.17}$$

Then in general, ζ_ρ gives the vertical displacement by internal waves, and $\zeta_T - \zeta_\rho$ and $\zeta_S - \zeta_\rho$ are measures of intrusive activity.

Figure 9.20 shows the situation in (T, S)-space. In the combined case, a projection parallel to the isopycnals can separate the two effects. For constant a and b, it is convenient to introduce a family of lines that are orthogonal to the lines of equal potential density (Veronis, 1972). They are here designated by π, for "spiciness" (hot and salty[10]), and they give a measure of the strength of the intrusion. The construction in (ρ, π)-space has some convenient properties. If the x- and y-axes are scaled in equivalent density units, bS and aT, then

$$\delta\rho = -aT + bS, \qquad \delta\pi = aT + bS. \tag{9.18}$$

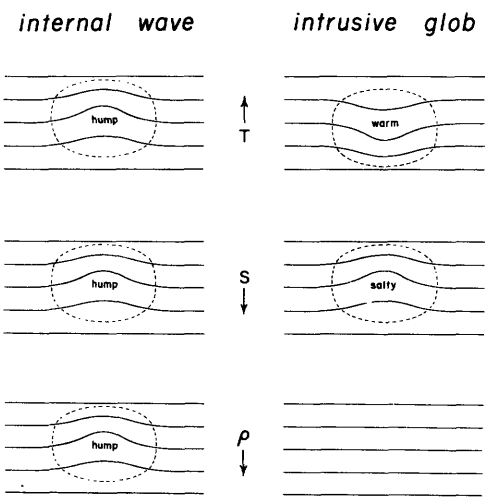

Figure 9.19 Contours of potential temperature, salinity and potential density in a vertical section (x, z) for an internal wave hump and a compensated warm and salty intrusive glob.

Figure 9.21 shows plots of the inferred vertical displacements in an area 200 miles southwest of San Diego (Johnson, Cox, and Gallagher, 1978). ζ_T, ζ_S, and ζ_ρ should all be alike for the case of a fine structure due to internal waves only [equation (9.17)], and this turns out to be the case down to a depth of 225 m. There is a broad intrusion between 225 and 260 m, and a narrow intrusion at 275 m. From a spectral analysis it was found that internal waves dominated the fine structure for all vertical scales that could be resolved, that is, down to 5 m.

The displacement spectrum in vertical wavenumber m steepens from approximately m^{-2} for $m < m_u$ to m^{-3} for $m > m_u$, with m_u near 0.6m^{-1} (~0.1 cpm). This kink appears to be a common feature in temperature spectra (Gregg, 1977; Hayes, 1978), and is most clearly portrayed in the temperature-gradient spectra (figure 9.22). A similar steepening is found in the spectrum of currents and current shear, but at a somewhat lower vertical wavenumber (Hogg, Katz, and Sanford, 1978).

A free-fall instrument called the "camel" for measuring the velocity microstructure has been developed by Osborn (1974; see chapter 14). Figure 9.23 presents measurements in the Atlantic Equatorial Undercurrent during the GATE experiment (Crawford and Osborn, 1980). The most intense microstructure of temperature and current was found above the velocity core. The microstructure in the core was weak and intermittent. Moderately intensive microstructure was found below the core, near the base of the thermocline. This is shown in great detail in figure 9.24. As an example, between 81 and 82 m there is an active temperature microstructure with positive and negative $\partial_z T$, accompanied by an active velocity microstructure. Similar evidence is found in horizontal tows, as for example in the upper part of figure 9.25 (Gibson, Schedvin, and Washburn, personal communication; see Gibson, 1980). The important conclusion is that velocity microstructure and small-scale temperature inversions must be closely linked, for one is not found without the other.

Occasionally one encounters patches of temperature microstructure without velocity microstructure. The inference is that these patches are the remains of a mixing event for which the velocity microstructure has decayed (fossil turbulence). Examples are found in the vertical profiles (figure 9.24 between 69 and 70 m depth), and in the horizontal tows (figure 9.25, bottom). But for the vertical profiles the temperature microstructure is here limited to only positive $\partial_z T$; the authors suggest that this might be a peculiarity of the core (velocity and salt) of the undercurrent.

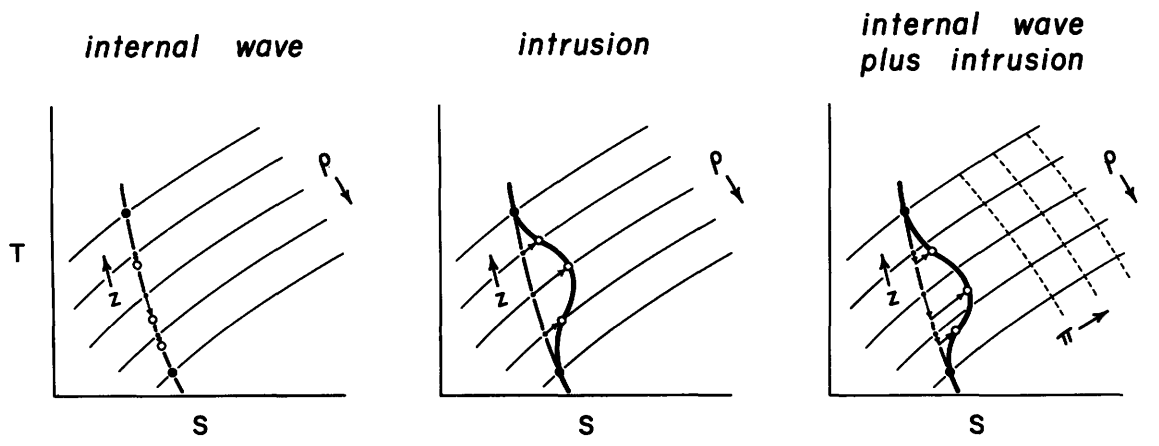

Figure 9.20 T-S relations for an internal wave hump and a compensated intrusive glob. The dots (•) correspond to the undisturbed positions of the five contours in figure 9.19. The open circles (○) give the positions through the center of the disturbance. The "isospiceness" lines (constant π) are orthogonal to the isopycnals (constant ρ).

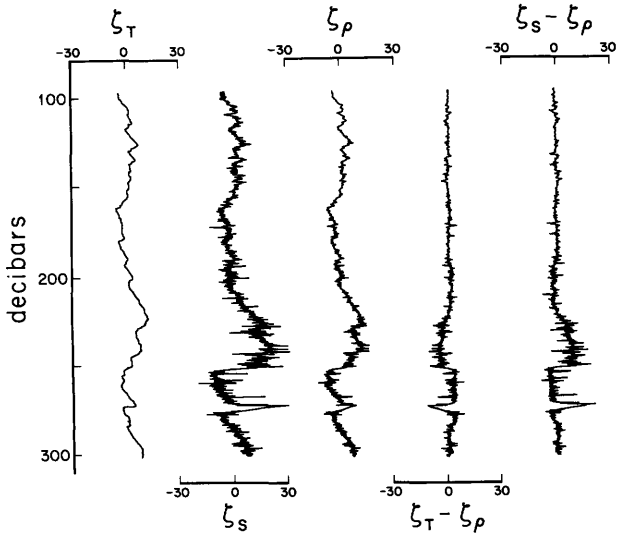

Figure 9.21 Displacement profiles in meters as inferred from the temperature, salinity, and density profiles. These should be alike for internal wave produced fine structure. The mean T and S gradients were of opposite sign (as in figure 9.19), hence the opposite signs of $\zeta_T - \zeta_\rho$ and $\zeta_S - \zeta_\rho$. (Johnson, Cox, and Gallagher, 1978.)

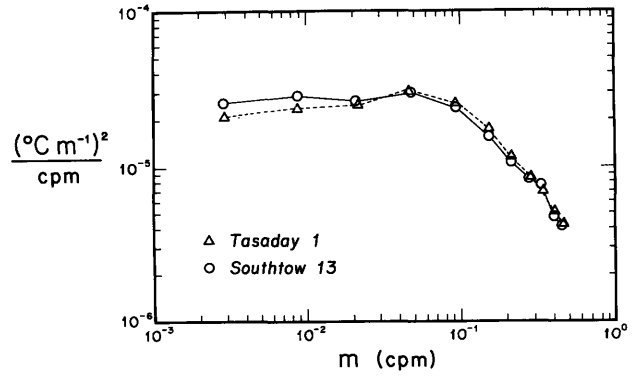

Figure 9.22 Temperature gradient spectra for two stations in the North Pacific. (Gregg, 1977.)

Crawford and Osborn have calculated the dissipation rates. Typical values just beneath the core of the undercurrent range from $\epsilon = 10^{-4}$ to 10^{-3} cm^2 s^{-3} (10^{-5} to 10^{-4} W m^{-3}). (Measurements away from the equator fall within the same limits.) But Belyaev, Lubimtzev, and Ozmidov (1975) obtain dissipation rates in the area of the undercurrent from horizontal tows that are higher by two orders of magnitude.[11]

The question of the relative magnitudes of vertical and horizontal scales has been examined by Hacker (1973) from a comparison of wing tip and nose temperatures of a rotating free-fall instrument. The horizontal separation is 1.7 m. The two records are coherent for vertical wavelengths down to 1 m. At smaller wavelengths the analysis is made difficult by the random tilts (5° rms) associated with internal waves. By selectively analyzing depth ranges of small tilts, Elliott and Oakey (1975) found coherence over a horizontal spacing of 0.5-m down to 10-cm vertical wavelengths. The conclusion is that anisotropy extends beyond the fine structure into the microstructure, perhaps as far as the dissipation scale (~1 cm).

The picture that emerges is one of a fine structure that is usually dominated by internal wave straining and is fairly uniform, in contrast to a microstructure that is extremely patchy and variable even in the mean. Patches of temperature microstructure without velocity microstructure ("fossil turbulence") evidently mark the demise of internal waves that had previously broken.

9.9 An Inconclusive Discussion

Is there a connection between internal wave activity, dissipation, and buoyancy flux? What is the explanation for the seeming steadiness of the internal wave field? Having gone this far, I cannot refrain from continuing with some speculation. The reader is encouraged to go no further (if he has gotten this far).

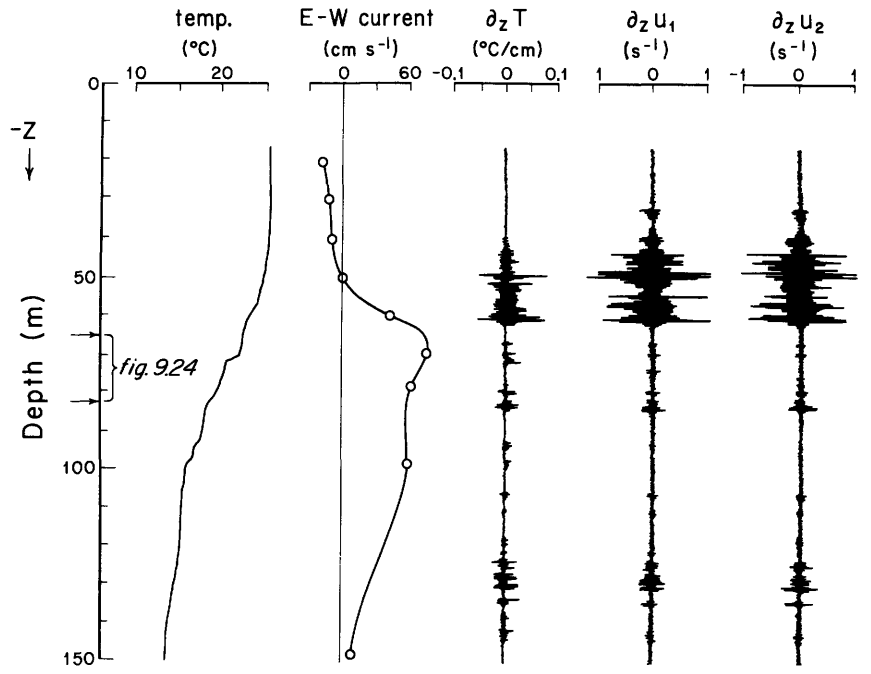

Figure 9.23 Temperature and velocity microstructure in the Atlantic Equatorial Undercurrent at 0°18'S, 28°01'W. (Crawford and Osborn, 1980.) The large scale-current profile was measured by J. Bruce. The region between 65 and 82 m is shown on an enlarged scale in figure 9.24.

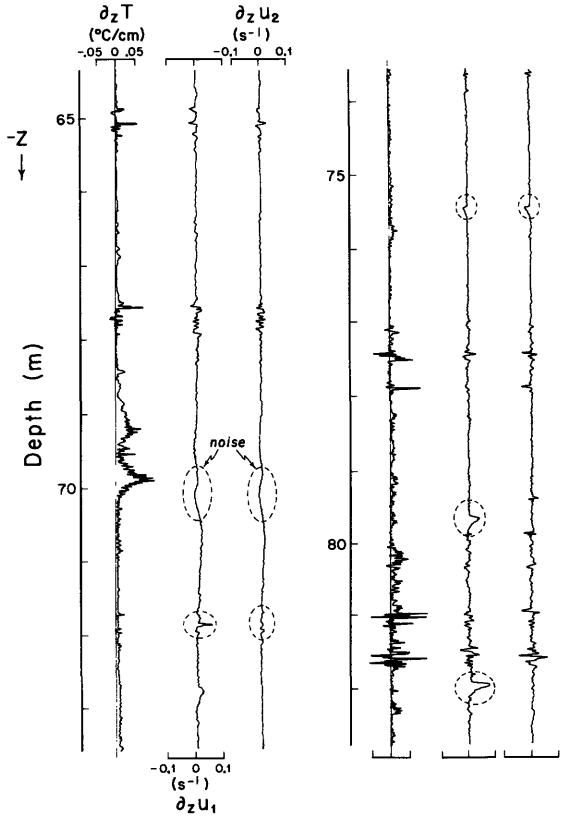

Figure 9.24 An enlarged section of the microstructure profile shown in figure 9.23. The encircled features have been attributed to various sources of instrumental noise.

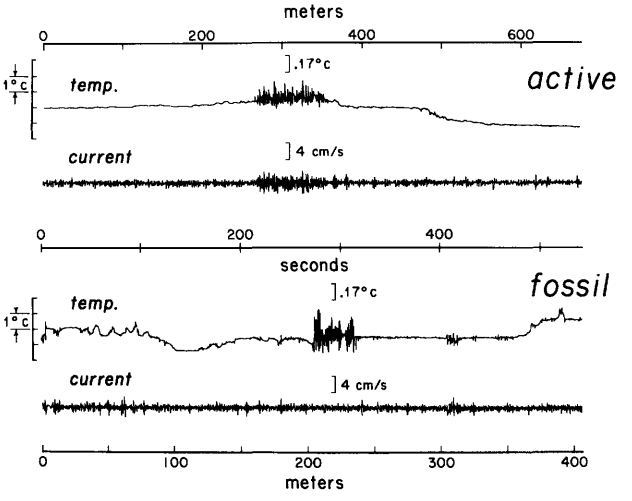

Figure 9.25 Active and fossil turbulence from towed body measurements during the mixed-layer experiment (MILE) in September 1977 near ocean station PAPA. The body was towed in the seasonal thermocline at a depth of 33 m; note the horizontal temperature change by about 0.3°C across the patches. The 1°C scale (left) refers to frequencies $f < 1$ H_z; the 0.17°C scale is for 1-12 H_z.
(I am indebted to C. Gibson, J. Schedvin, and L. Washburn for permission to show these measurements. See also Gibson, 1980.)

We shall need some quantitative guidance for internal wave intensities. For that purpose I shall use the model spectrum of Garrett and Munk (1972b, 1975, 1979), with slight modifications. The model fails near the ocean boundaries[12] (Pinkel, 1975). The spectrum was developed on the basis of rank empiricism, with no trace of underlying theory. But it has since gained some respectability by the theoretical findings of Watson and collaborators that the shape of the GM spectrum is stable to nonlinear interactions, except for the lowest modes and near-inertial frequencies [Meiss, Pomphrey, and Watson (1979); Pomphrey, Meiss, and Watson (1980); see also McComas (1977)].

9.9.1 Model Spectrum GM79

The internal wave energy is assumed to be equally distributed in all horizontal directions, so that only a single horizontal wavenumber, $k = (k_1^2 + k_2^2)^{1/2}$, is used. Upward and downward energy flux are taken as equal. The spectra of vertical displacement, horizontal velocity, and energy per unit mass are[13]

$$F_\zeta(\omega,j) = b^2 N_0 N^{-1}(\omega^2 - f^2)\omega^{-2}E(\omega,j), \tag{9.19}$$

$$F_u(\omega,j) = F_{u_1} + F_{u_2} = b^2 N_0 N(\omega^2 + f^2)\omega^{-2}E(\omega,j), \tag{9.20}$$

$$F_e(\omega,j) = \tfrac{1}{2}(F_u + N^2 F_\zeta) = b^2 N_0 N E(\omega,j), \tag{9.21}$$

where j is the vertical mode number, $b \approx 1.3$ km the e-folding scale of $N(z)$, with $N_0 \approx 5.2 \times 10^{-3}\,\mathrm{s}^{-1}$ (3 cph) the surface-extrapolated buoyancy frequency and $f = 7.3 \times 10^{-5}\,\mathrm{s}^{-1}$ the Coriolis frequency at lat. 30°. We can ignore F_w compared to F_u. At high frequencies, $\omega \gg f$, kinetic and potential energy densities are equal: $\frac{1}{2}F_u = \frac{1}{2}N^2 F_\zeta$. $E(\omega,j)$ is a dimensionless energy density that is factored as follows:

$$E(\omega,j) = B(\omega)\cdot H(j)\cdot E,$$

$$B(\omega) = 2\pi^{-1} f \omega^{-1}(\omega^2 - f^2)^{-1/2}, \qquad \int_f^{N(z)} B(\omega)\,d\omega = 1,$$

$$H(j) = \frac{(j^2 + j_*^2)^{-1}}{\sum_1^\infty (j^2 + j_*^2)^{-1}}, \qquad \sum_{j=1}^{\infty} H(j) = 1.$$

The factor $(\omega^2 - f^2)^{-1/2}$ in the expression for $B(\omega)$ is a crude attempt to allow for the peak at the inertial turning frequency (see figure 9.11); $j_* = 3$ is a mode scale number, and E is the internal wave "energy parameter." We set

$$E = 6.3 \times 10^{-5} \qquad \text{(dimensionless)}. \tag{9.22}$$

There is a surprising universality[14] to the value of E (mostly within a factor of two).

The transfer into (ω,k)- or (ω,m)-space is accomplished by setting $F(\omega,j)\,\delta j = F(\omega,k)\,dk = F(\omega,m)\,dm$, with

$$m = k\left(\frac{N^2 - \omega^2}{\omega^2 - f^2}\right)^{1/2} = \pi b^{-1}\left(\frac{N^2 - \omega^2}{N_0^2 - \omega^2}\right)^{1/2} j \tag{9.23a}$$

for a slowly varying $N(z)$, in accord with the WKB approximation [equations (9.4) and (9.7)]. For most purposes we can ignore the situation near the buoyancy turning frequency,[15] so that

$$m \approx kN(\omega^2 - f^2)^{-1/2} \approx \pi b^{-1}(N/N_0)j. \tag{9.23b}$$

For the sake of simplicity, the energy spectrum has been factored into $B(\omega)\cdot H(j)$. But there is evidence from Pinkel (1975) and from the IWEX measurements (Müller, Olbers, and Willebrand, 1978) that there is relatively more energy in the low modes at high frequency, and this could account for the astounding vertical coherences found by Pinkel in the upper 400 m at high frequencies.

I have no doubt that further discrepancies will be found; still, I believe that the model can now give useful quantitative estimates. For example, according to "Fofonoff's rule" (he disclaims ownership), the mean-square current within a 1-cph band centered at 1 cph is $1\,\mathrm{cm}^2\,\mathrm{s}^{-2}$; this compares to $F_u(1\text{ cph}) = 0.8\,\mathrm{cm}^2\,\mathrm{s}^{-2}\,(\mathrm{cph})^{-1}$ from (9.20). This agreement is not an accident, of course, the GM model having been based, in part, on the site D measurements (Fofonoff, 1969).

The mean-square quantitites are likewise in accord with the usual experience. From (9.19), (9.20), and (9.21),

$$\begin{aligned}
\langle \zeta^2 \rangle &= \int d\omega \sum F_\zeta(\omega,j) \\
&= \tfrac{1}{2} b^2 E N_0 N^{-1} = 53(N/N_0)^{-1}\,\mathrm{m}^2, \\
\langle u^2 \rangle &= \langle u_1^2 \rangle + \langle u_2^2 \rangle = \int d\omega \sum F_u(\omega,j) \\
&= \tfrac{3}{2} b^2 E N_0 N = 44(N/N_0)\,\mathrm{cm}^2\,\mathrm{s}^{-2}, \\
\hat{E}(z) &= \int d\omega \sum F_e(\omega,j) \\
&= b^2 E N_0 N = 30(N/N_0)\,\mathrm{cm}^2\,\mathrm{s}^{-2},
\end{aligned} \tag{9.24}$$

giving 7 m for the rms vertical displacement and $7\,\mathrm{cm\,s}^{-1}$ for the rms current in the upper oceans beneath the mixed layer. The energy can be written alternatively $\hat{E}(z) = \frac{1}{2}[\langle u^2 \rangle + N^2 \langle \zeta^2 \rangle]$ so that the *total* kinetic energy is three times the total potential energy in the GM model. $\rho\hat{E}(z)$ is the energy per unit volume; the energy per unit area is

$$\begin{aligned}
\rho\hat{E} &= \int \rho\hat{E}(z)\,dz = \rho b^2 E N_0 \int N\,dz = \rho b^2 E N_0 \int b\,dN \\
&\approx \rho b^3 N_0^2 E \\
&= 3.8 \times 10^6\,\mathrm{erg\,cm}^{-2} = 3800\,\mathrm{J\,m}^{-2},
\end{aligned}$$

using $b^{-1} = N^{-1}\cdot dN/dz$ as definition for the e-folding scale b.

9.9.2 Universality

It has turned out, quite unexpectedly, that the intensities are remarkably uniform in space and time.

Wunsch (1976) has made a deliberate attempt to find systematic deviations for a variety of deep water locations in the North Atlantic, with the purpose of identifying sources and sinks of internal wave energy. Using the frequency band $\frac{1}{8}$ to $\frac{1}{4}$ cph as a standard, the only clear deviations he could find were associated with topographic features, particularly Muir Seamount, and even these were inconspicuous at short distance. In a further study (Wunsch and Webb, 1979) some evidence is presented for deviations on the equator and in regions of high mean shear.

Figure 9.26 shows a continuing spectral display over an 18-day period, and this is found consistent with a stationary Gaussian process (Cairns and Williams, 1976). [The mean distribution is in accord with the equation (9.19) for $F_\zeta(\omega) = \Sigma F_\zeta(\omega,j)$, setting $\Sigma H(j) = 1$.] These observations were taken during 21 days of mild to moderate winds. Davis (personal communication) has recorded currents in the seasonal thermocline over a 19-day interval with two periods of heavy winds (figure 9.27). The first event is followed in about 2 days by an increase in mean-square currents, the second event in somewhat less time. Energy enhancement is by a factor of three or less. Johnson, Cox, and Gallagher (1978) found a temporarily elevated spectral level on a windy day. Following these events, the intensities rapidly relax to their normal state.

9.9.3 Generation

The observed growth times are consistent with a theory for the generation of internal waves by resonant interaction with surface waves (Brekhovskikh, Goncharov Kurtepov, and Naugol'nykh, 1972; Watson, West, and Cohen, 1976).

But there are other means of generating internal waves. Garrett (1979) has reviewed a variety of contenders, all of which fall (surprisingly) into the right order of magnitude. For reference, he takes $7 \times 10^{-3}\,\mathrm{W\,m^{-2}}$ for the internal wave dissipation (corresponding to a relaxation time of one week). Globally, this amounts to 2 TW (terawatts: tera = 10^{12}). The total loss of energy of the earth-moon system is known from the moon's orbit to be 4 TW, mostly by tidal dissipation in the oceans. It is not impossible that surface tides pump significant amounts of energy into internal wave motions via internal tides (cf. chapter 10). Other contenders are surface forcing by traveling fluctuations of wind stress and buoyancy flux, currents over bottom topography, and extraction from the mean current shear. There is no problem with supplying internal waves with 2 TW of power; the problem is rather to eliminate some of the potential donors.

9.9.4 Instability

We can now derive some numerical estimates for a variety of instability parameters. The spectrum $F_{u'/N}$ of

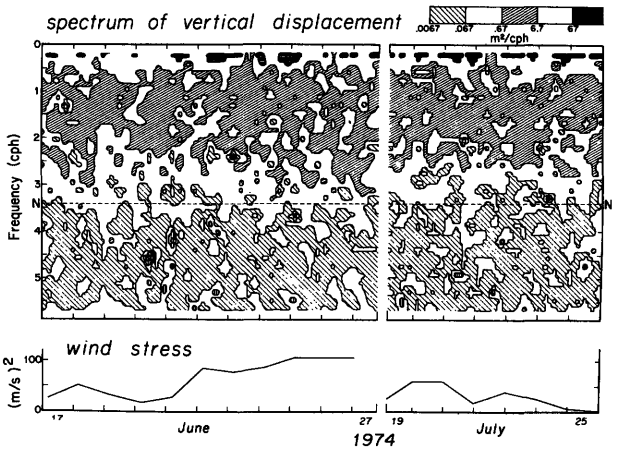

Figure 9.26 Time-frequency display of $F_\zeta(\omega)$ from MISERY 1 and MISERY 3. (Cairns and Williams, 1976.) $\zeta(t)$ is the depth of the 6.60° isotherm (at a mean depth of 350 m) in a location 800 km offshore of San Diego, California, measured with a yo-yoing midwater capsule. The squared wind (bottom) shows light winds at the start and end of the experiments.

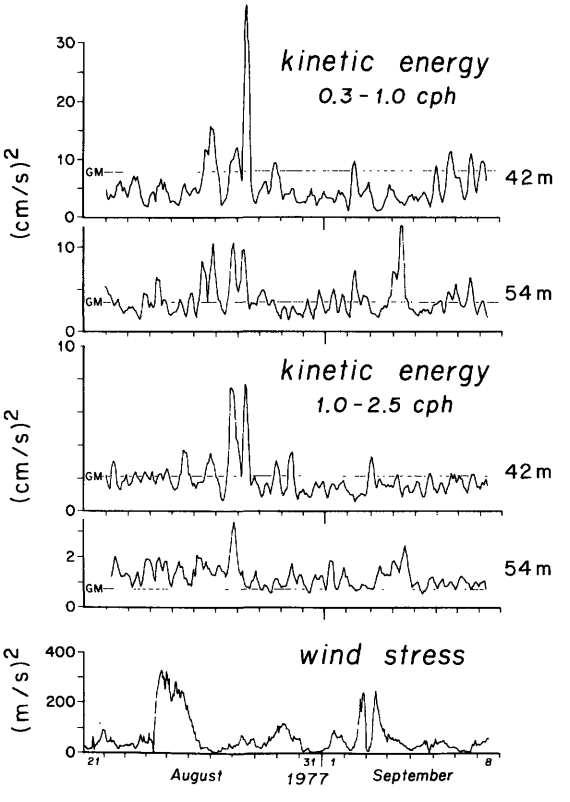

Figure 9.27 Kinetic energy $\langle u^2 \rangle = \langle u_1^2 \rangle + \langle u_2^2 \rangle$ during the mixed-layer experiment (MILE) on station PAPA (50°N, 145°W) at 42 and 54 m depths. The upper two plots refer to a frequency band of 0.3 to 1.0 cph, the next two plots to a band 1.0 to 2.5 cph. The squared wind (bottom) shows two episodes of large wind stress. The GM model levels are indicated [using N = 0.023, 0.0096 $\mathrm{s^{-1}}$ (13, 5.5 cph) at 42, 54 m], though the model is not really applicable to such shallow depths and sharp N-gradients. (I am indebted to R. Davis for permission to use his measurements.)

the reciprocal Richardson number is defined by

$$Ri^{-1} = \langle |u'|^2 \rangle / N^2 = \int d\omega \sum_j F_{u'/N}(\omega, j),$$

where $\langle |u'|^2 \rangle = \langle |\partial_z u_1|^2 \rangle + \langle |\partial_z u_2|^2 \rangle = m^2 \langle u^2 \rangle$. But $m = \pi b^{-1}(N/N_0)j$ (9.23b) and so

$$F_{u'/N} = 2\pi E(N/N_0) f(\omega^2 + f^2)\omega^{-3}(\omega^2 - f^2)^{-1/2} j^2 H(j). \quad (9.25)$$

The principal contribution comes from the inertial frequencies. Performing the ω-integration,

$$Ri^{-1} = \tfrac{3}{2}\pi^2 E(N/N_0) \sum j^2 H(j). \quad (9.26)$$

We now perform the mode summations (subscript u for upper)

$$\sum_{j=1}^{j_u} j^2 (j^2 + j_*^2)^{-1} \approx j_u,$$

$$\sum_{j=1}^{j_u} (j^2 + j_*^2)^{-1} \approx \tfrac{1}{2} j_*^{-2} (\pi j_* - 1) \equiv J^{-1} = 0.47$$

for $j_u \gg j_* = 3$. The spectrum $F_{u'/N}(j)$ is white (except for the lowest few mode numbers) and Ri^{-1} depends on the choice of the upper cutoff j_u. In terms of the limiting vertical wavenumber $m_u = \pi b^{-1}(N/N_0) j_u$ we have, finally,

$$Ri^{-1} = \tfrac{3}{2}\pi J E m_u b. \quad (9.27)$$

If we identify m_u with the kink (figure 9.22) at $0.6 m^{-1}$ (0.1 cpm), then $Ri^{-1} = 0.52$. If the spectrum is extended beyond the break, with a slope m^{-1} to some new upper limit $m_{uu} = 10 m_u$ (say), then $Ri^{-1} = 0.52(1 + \ln m_{uu}/m_u) = 1.72$. Hogg, Katz, and Sanford (1978) find Ri^{-1} near 0.5 in the open ocean near Bermuda, including m up to 0.2 cpm. An interesting scatter plot has been produced by Eriksen (1978) and is shown in figure 9.28. The conclusion is that the internal-wave shear field is associated with Richardson numbers of order 1:

$$Ri^{-1} = \text{order}(1). \quad (9.28)$$

We can proceed in a similar manner with regard to advective instability. The simplest generalization of the earlier discussion (section 9.7) is to derive the spectral decomposition of $\langle u^2/c^2 \rangle$, $c = \omega/k$. (Would $\langle u^2 \rangle / \langle c^2 \rangle$ be better?) The equations of continuity and of dispersion (away from the turning frequencies) can be written

$$k\xi + m\zeta = 0, \quad c = \omega/k = N/m,$$

so that

$$\frac{u}{c} = \frac{mu}{mc} = \frac{u'}{N}.$$

Similarly, for horizontal and vertical strain,

$$\partial\xi/\partial x = -\partial\zeta/\partial z = ik\xi = (k/\omega)u = u/c.$$

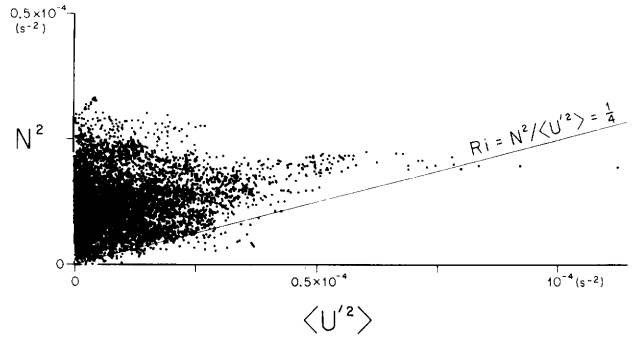

Figure 9.28 A scatter plot of squared shear (over 6.3 m vertical separation) versus N^2 (over 7.1 m) of estimates made every 40 s for 78 hours. (Eriksen, 1978.) Eriksen finds that Ri rarely falls below the critical value $\frac{1}{4}$, and that $\phi = \tan^{-1} Ri$ is uniformly distributed for ϕ greater than $\tan^{-1}(\frac{1}{4})$.

Thus shear, advection, and longitudinal strains all have similar conditions for instability, and we can write

$$\langle \phi^2 \rangle = CEm_u b \quad (9.29)$$

for any of these, without having to go into gruesome details. [Integrations yield $C = 2.5, 5.8, 3.3, 3.3$ for $u'/2N$, u/c, $\partial_x\xi$, $\partial_z\zeta$, respectively; this is a spectrally weighted version of the Orlanski and Bryan argument [equation (9.16)] that advective instability is the most likely to occur.]

9.9.5 Compliant Wave Cutoff

The instability condition $\langle \phi^2 \rangle = \text{order}(1)$ is an argument for a universal value of the product Em_u. To account for a universal E we need some additional condition.

I propose that the upper cutoff m_u is related to the transition at $c_c \approx N/m_c = \text{rms}\, u$ from the intrinsic to the compliant parts of the internal wave spectrum:

$$m_u = C' m_c = C' N/\text{rms}\, u, \quad (9.30)$$

where C' is a constant of order (1). It stands to reason that the strongly interacting high wavenumbers have a different spectral form from the intrinsic waves. If we identify m_u with the kink (figure 9.22) at $0.6\ \text{m}^{-1}$ (0.1 cpm), then for $N = 0.01\ \text{s}^{-1}$ and $\text{rms}\, u = 10\ \text{cm s}^{-1}$ this gives $C' = 6$ (somewhat large for comfort).

There is an equivalent way of postulating the upper cutoff. The ϕ-spectrum is white up to some limit which is the reciprocal of the vertical extent Δ of the smallest ϕ-features. One might suppose this vertical extent to be some given fraction of the rms *amplitude* of the internal waves. (White caps occupy some fraction of the surface wave crests; the distance between crests is not a critical factor.) Using the foregoing numbers, we can write

$$\Delta = m_u^{-1} = 1.37(C')^{-1}\, \text{rms}\, \zeta = 0.23\, \text{rms}\, \zeta = 1.7\ \text{m}. \quad (9.31)$$

From the expressions (9.24) for $\langle \zeta^2 \rangle$ and $\langle u^2 \rangle$, either condition (9.30) or condition (9.31) leads to an energy parameter

$$E = [\langle \phi^2 \rangle / CC']^2 N_0/N. \tag{9.32}$$

For $C = 5$, $C' = 6$, $E = 10^{-3}\langle \phi^2 \rangle^2 N_0/N$. Then with $\langle \phi^2 \rangle$ a moderate fraction of its critical value 1, we can recover the numerical value $E = 6 \times 10^{-5}$. This is not to say that E has been calculated from first principles; it is only to say that acceptable values for the various coefficients lead to a small numerical value of the dimensionless energy parameter, as observed.

9.9.6 Dissipation

For small numerical values of the instability parameter $\langle \phi^2 \rangle$ we are in a regime of *sparse* instabilities in space and time (such as incipient whitecaps in light winds). When $\langle \phi^2 \rangle$ is near 1 the probability for instabilities is high. For an a priori estimate of $\langle \phi^2 \rangle$ we require (1) a model to relate $\langle \phi^2 \rangle$ to the internal wave energy dissipation, and (2) an estimate of the rate of dissipation (or generation for a given steady state). This is essentially the procedure followed by Longuet-Higgins (1969a) in his stimulating attempt to interpret the Phillips saturation constant for surface waves.

Perhaps the simplest scheme is to relate the dissipation to the probability for $\phi > 1$.[16] The variance of ζ associated with $\phi > 1$ is $\langle \zeta^2 \rangle \cdot p\ (\phi > 1)$ for uncorrelated ζ and ϕ (as when $\phi = \partial_z \zeta$). Potential energy is proportional to $\langle \zeta^2 \rangle$; accordingly the rate of fractional energy dissipation can be written

$$\frac{1}{E}\frac{dE}{dt} = -\sigma p(\phi > 1), \tag{9.33}$$

where σ^{-1} is the characteristic interval during which the energy associated with $\phi > 1$ is lost to the organized wave field and renewed by generation processes. For a rough estimate (Garrett and Munk, 1972a),

$$\sigma^2 = \pi^{-2}\int_f^N \omega^2 F_\phi(\omega) d\omega \Big/ \int_f^N F_\phi(\omega) d\omega$$
$$\approx \pi^{-2} f N \tag{9.34}$$

for any of the ϕ-spectra [such as (9.25)]. A Gaussian ϕ-distribution $p(\phi) = \pi^{-1/2}\beta \exp(-\beta\phi^2)$ leads to

$$p\ (\phi > 1) \approx \pi^{-1/2}\beta^{-1/2} \exp(-\beta), \qquad \beta \equiv \frac{1}{2\langle \phi^2 \rangle}, \tag{9.35}$$

provided β is large. In the upper ocean $\sigma = 20$ per day, and $\beta = 2.1$, 3.7, for relaxation times of 1 day, 1 week, respectively. The foregoing numerical values are not important; what is significant is that a tenfold increase in the rate of dissipation (and generation) is accompanied by only a threefold increase in β^2 (and hence in wave energy). Thus the energy level stays within rather narrow limits even though generation and dissipation processes may vary widely, particularly for large β. We propose for a "universality hypothesis" that the energy level responds only logarithmically to variable forcing. We shall examine this situation in more detail.

9.9.7 The Energy Balance

The differential equation of wave energy can be written

$$dE/dt = G(t) - D(t),$$

where $G(t)$ and $D(t)$ are the rates of energy generation and dissipation. We use the notation $\tilde{E}$, $\tilde{G}$, $\tilde{D}$ to represent the "normal" state of internal wave statistics. From (9.32) and (9.35)

$$E \sim \beta^{-2}(N_0/N), \qquad D \sim \beta^{-1/2} e^{-\beta},$$

with $\tilde{D} = \tilde{G}$. We define the relaxation time

$$\tilde{t} = \tilde{E}/\tilde{G};$$

accordingly $\tilde{t}^{-1}$ is the initial rate of decay for a wave field in equilibrium with $\tilde{G}$ if the generation is suddenly turned off. The differential energy equation can now be written

$$\frac{d\mathscr{E}}{d\tau} + \mathscr{E}^{1/4} \exp[\tilde{\beta}(1 - \mathscr{E}^{-1/2})] = g(\tau),$$
$$\tilde{\beta} = \tilde{E}^2 (N/N_0)^{-1/2}, \tag{9.36}$$

where

$$\mathscr{E}(\tau) = E/\tilde{E}, \qquad g(\tau) = G/\tilde{G}, \qquad \tau = t/\tilde{t},$$

with

$$\langle \mathscr{E} \rangle = 1, \qquad \langle g \rangle = 1.$$

For large $\mathscr{E}$, the dissipation is $\mathscr{E}^{1/4} \exp \tilde{\beta}$ and thus large; for small $\mathscr{E}$, it is $\mathscr{E}^{1/4} \exp -(\tilde{\beta}\mathscr{E}^{-1/2})$ and thus very small.

The problem is to derive properties of the energy statistics for given generation statistics. (This is related to the fluctuation-dissipation theorem in the study of Brownian motion.) Two special solutions are easily found. For an equilibrium situation, (9.36) with $d\mathscr{E}/d\tau = 0$ gives the values $\mathscr{E}(g;\beta)$ in table 9.2. Departures from the normal state in E are much smaller than those in g, particularly at large β and for small g's.

To obtain some feeling for the nonlinear response time, let $g(\tau)$ go abruptly from 1 to g at time 0, and set $\mathscr{E}(\tau) = 1 + \epsilon(\tau)$, with $\epsilon \ll 1$ (but *not* $\epsilon\tilde{\beta} \ll 1$). Equation (9.36) becomes

$$dz/d\tau' + z^2 = gz, \qquad z = \exp(\tfrac{1}{2}\tilde{\beta}\epsilon), \qquad \tau' = \tfrac{1}{2}\tilde{\beta}\tau,$$

with the solution

$$\tau = \frac{2}{\tilde{\beta}g} \ln \frac{(g-1)z}{g-z}.$$

For the case $g \to 0$, $\tau' \to z^{-1} - 1$, and

$$d\epsilon/d\tau = 2\tilde{\beta}^{-1} d \ln z/d\tau \to -z, \tag{9.37}$$

Table 9.2 Energy Equilibrium $\mathscr{E}(g;\beta)$ from (9.36) for $d\mathscr{E}/d\tau = 0$ (top), Dimensionless Response Time $\tau_{1/2}$ (9.38) for an Abrupt Change in Generation from 1 to g (center), Relaxation Time $\tau_{1/2}$ (9.39) for a Change from g to 1 (bottom)[a]

		g (dB)				
		−10	−5	0	5	10
	Energy levels in dB					
	2	−6.0	−3.4	0	4.9	13.0
$\tilde{\beta}$	5	−3.0	−1.7	0	2.0	4.6
	10	−1.7	−0.9	0	1.0	2.1
	Response time (dimensionless)					
	2	2.75	1.41	0.69	0.32	0.14
$\tilde{\beta}$	5	1.10	0.56	0.28	0.13	0.06
	10	0.55	0.28	0.14	0.06	0.03
	Relaxation time (dimensionless)					
	2	1.43	1.02	0.69	0.45	0.27
$\tilde{\beta}$	5	0.57	0.41	0.28	0.18	0.11
	10	0.29	0.20	0.14	0.09	0.05

a. Generation g and energy $\mathscr{E}$ are in decibels relative to normal levels.

in accord with $d\epsilon/d\tau = -1$ for the initial rate of decay. As τ goes from 0 to ∞, z goes from 1 to g, and ϵ from 0 to $2\tilde{\beta}^{-1}\ln g$. Half energy response is for $\epsilon = \tilde{\beta}^{-1}\ln g$, $z = g^{1/2}$, and

$$\tau_{1/2} = 2\tilde{\beta}^{-1}g^{-1}\ln(1 + g^{1/2}). \tag{9.38}$$

For energy *relaxation*, going abruptly from g to 1 at time 0, the solution is

$$\tau = 2\tilde{\beta}^{-1}\ln\frac{(g-1)z}{g(z-1)}, \qquad \tau_{1/2} = 2\tilde{\beta}^{-1}\ln(1 + g^{-1/2}). \tag{9.39}$$

Half-times $\tau_{1/2}$ are given in table 9.2. For a linear system these would all be the same. Here the times are shorter for internal wave storms ($g > 1$) and longer for calms ($g < 1$), and this variation is more pronounced in response to a change in generation from a normal to a perturbed level than for relaxation back to normal generation. (The assumption of weak nonlinearity for computing τ is violated in the columns for $g = \pm 10$ dB.)

The imperceptible decay of internal wave intensities during relatively low winds (figure 9.26) is consistent with half the normal energy, and the rapid decay following a blow (figure 9.27) requires perhaps three times normal energy. If we can count on a storm or some other generation event to "top up" the internal wave energy once every hundred days, then we may expect the wave energies to remain generally within a factor of two.

I have paid no attention to depth dependence. The dissipation can be written

$$\hat{D} = \sigma(\pi\beta)^{-1/2}\exp(-\beta)\hat{E},$$

where $\rho\hat{D}(z)$, $\rho\hat{E}(z)$ are the dissipation and energy per unit volume, respectively. The dependence on depth is through

$$\sigma \sim n, \qquad \beta \sim n^{-1/2}, \qquad \hat{E} \sim n,$$

with $n(z) = N(z)/N_0$; hence

$$\hat{D} = \hat{D}_0\beta^{-9/2}\exp(\beta_0 - \beta), \qquad \hat{E} = \hat{E}_0\beta^{-2}.$$

Writing $dz = b\,dn/n = -2b\,d\beta/\beta$,

$$\int \hat{D}\,dz = 2b\hat{D}_0\int \beta^{-11/2}\exp(\beta_0 - \beta)\,d\beta,$$

$$\int \hat{E}\,dz = 2b\hat{E}_0\int \beta^{-3}\,d\beta.$$

Integrating from the surface ($\beta = \beta_0$) to the bottom ($\beta \approx \infty$), the integrals for large β_0 (as previously assumed) give

$$\int \hat{D}\,dz = 2b\hat{D}_0\beta_0^{-11/2}, \qquad \int \hat{E}\,dz = b\hat{E}_0\beta_0^{-2}$$

with an "integral relaxation time"

$$\tfrac{1}{2}\beta_0^{7/2}\hat{E}_0/\hat{D}_0 = \tfrac{1}{2}\pi^{1/2}\beta_0^{\frac{1}{2}}e^{\beta_0}\sigma_0^{-1}. \tag{9.40}$$

Suppose the generation takes place in the upper few hundred meters, so that the dissipation in the interior ocean is compensated by downward radiation of internal wave energy. From a rotary decomposition of current profiles, Leaman (1976) estimates a downward flux of order $10^{-4}\,\mathrm{W\,m^{-2}}$. We compare this with the integrated dissipation beneath a scale depth $z = -b = -1.3$ km (where $n = e^{-1}$ and $\beta = \beta_0\sqrt{e}$):

$$\rho\int_{\beta_0\sqrt{e}}^{\infty}\hat{D}(z)\,dz = 2\pi^{-1/2}e^{-11/4}\beta_0^{-6}e^{-\beta_0}\sigma_0N_0^2\rho b^3\tilde{E},$$

where $\tilde{E}$ is the "normal" dimensionless energy parameter. The result is $\beta_0 = 2.1$. The corresponding integral relaxation time [equation (9.40)] is 7 days. The normal surface relaxation time is

$$\tilde{t}_0 = \hat{E}_0/\hat{D}_0 = (\pi\beta_0)^{1/2}e^{\beta_0}\sigma_0^{-1} = 1.1 \text{ days}.$$

The dimensionless times in table 9.2 can be interpreted as shallow response times in days.

The strong dependence of dissipation on depth is an inherent feature of the proposed phenomenology.

9.9.8 Mixing

The balance between production and dissipation of turbulent energy can be represented by

$$\mu = \epsilon = \epsilon_p + \epsilon_k. \tag{9.41}$$

$\rho\epsilon_p$ is the rate of production of potential energy, e.g., the *buoyancy flux* $g\langle w'\rho'\rangle$, with the primes designating the fluctuating components; $\rho\epsilon_k$ is the dissipation of kinetic energy into heat. The fraction of work going

into potential energy is the flux Richardson number Rf:

$$Rf = \epsilon_p/\mu = \epsilon_p/\epsilon. \tag{9.42}$$

$Rf < 1$ in order for $\epsilon_k > 0$. We have previously discussed the evidence that something less than $\frac{1}{4}$ of the kinetic energy dissipated appears as potential energy. Taking a typical value $\epsilon_p/\epsilon_k = \frac{1}{5}$ (Thorpe, 1973b, p. 749) gives $Rf = \frac{1}{6}$. The eddy flux of density can be written in terms of the eddy diffusivity A: $\langle w'\rho' \rangle = A \cdot d\rho/dz = AN^2(g/\rho)^{-1} = \rho\epsilon_p/g$, and so

$$A = \frac{\epsilon_p}{N^2} = \frac{\epsilon}{N^2} Rf = \frac{\epsilon_k}{N^2} \frac{Rf}{1 - Rf}. \tag{9.43}$$

Our procedure is to estimate ϵ_p from internal wave breaking, and to compute A and ϵ from (9.43), using $Rf = \frac{1}{6}$. There are, of course, other sources of turbulence; Osborn (1980) stresses the work done by the ambient turbulence in a mean shear: $\mu = \langle u'w' \rangle du/dz$. His procedure is to estimate ϵ from the measured mean-square shear, and to compute A from (9.43).

The random superposition of internal waves leads to the intermittent occurrence of "traumata"[17] associated with $\phi > 1$. The traumata are the locus of incipient turbulence, and quickly spread to some thickness Δ within which the average ϕ is reduced from 1 to about 0.9 (Thorpe, 1973b). Subsequently the patch continues to grow to some maximum thickness Δ_{max} at the time the surrounding ϕ is largest, always keeping ϕ within the patch to 0.9.

The change of potential energy per unit surface area associated with perfect mixing over a depth Δ in a density gradient $d\rho/dz$ is $(1/12)g(d\rho/dz)\Delta^3 = (1/12)\rho N^2\Delta^3$. (Imperfect mixing just reduces the factor 1/12.) The average change of potential energy per unit time per unit volume is then

$$\rho\epsilon_p = \frac{1}{12} \rho N^2 \Delta^3 \nu,$$

where ν is the number of traumata per unit (t, z)-space. $\rho\epsilon_p$ equals the buoyancy flux $\rho N^2 A$ by definition of the eddy diffusivity A; hence

$$A = \frac{1}{12} \Delta^3 \nu.$$

I have previously identified Δ with m_u^{-1} [equation (9.31)]. For ν we write

$$\nu = m'\sigma p(\phi > 1), \qquad m' = 0.2m_u, \qquad \sigma \approx \pi^{-1}(fN)^{1/2},$$

where m' is the rms spacial frequency derived from an equation analogous to (9.34). Putting all this together,

$$A \approx 10^{-2}\Delta^2/T, \qquad T \equiv \sigma^{-1}\beta^{1/2}e^{\beta}, \tag{9.44}$$

where T is the expected time interval between events over a distance $1/m'$. This is of similar form as the result of Stommel and Fedorov (1967), as is inevitable for what is, after all, a mixing-length theory.

The principal conclusion is a strong dependence of A on depth, and on any departures from normal generation. The numerical value for the normal state is $\tilde{A} = 10^{-2}$ cm^2 s^{-1}, much lower than the global 1 cm^2 s^{-1}.

9.9.9 Saturation Spectra

There is an essential distinction between the usual formulation of turbulence and the saturation processes as here envisioned. We consider the regime of *sparse* instabilities in space and time (such as incipient whitecaps in light winds). Then the ϕ-field consists of scattered and uncorrelated spikes, and the ϕ-spectrum is accordingly white up to some limit that is the reciprocal of the vertical extent of the spikes. The dissipation is localized in physical space, and therefore broadly distributed in wavenumber space. In the usual turbulent situation, the dissipation is confined to a narrow (dissipation) region in wavenumber space, and spread in physical space.

A white spectrum in any of the ϕ-spectra, whether shear, advection or strain, implies an m^{-2} energy spectrum. The energy spectrum steepens (perhaps to m^{-3}) in the transition from the intrinsic to the compliant waves. Presumably the m^{-3} energy spectrum extends to the Ozmidov (or Richardson or Monin–Obukov) scale $m_0 = (N^3/\epsilon)^{1/2} \approx 4$ m^{-1} (about 0.6 cpm), which is conveniently close to the definition of the microstructure boundary, then flattens out to the Kolmogorov dissipation scale $m_k = (\epsilon/\nu^3)^{1/4} \approx 3$ cm^{-1} (0.5 cpcm), and finally cuts off exponentially (Gregg, Cox, and Hacker, 1973, figure 11). But such a description of "in-the-mean" scales may not be appropriate to a patchy environment, and is anyway beyond the scope of this survey.

9.10 Conclusion

I shall end as I started: the connection between internal waves and small scale processes—that is where the key is. I feel that we are close to having these pieces fall into place, and I am uncomfortable with having attempted a survey at this time.

Notes

1. They were found at Loch Ness at about the same time (Watson, 1904; Wedderburn, 1907).

2. The temperature measurements were made using a submarine cable from a recording Wheatstone bridge on the shore at Bermuda to two resistance thermometers offshore: both lay on the bottom, one at a depth of 50 m and the other at 500 m (Haurwitz, Stommel, and Munk, 1959).

3. Salinity is not directly measured, but has to be inferred from conductivity or sound speed, which are primarily responsive to temperature. This large temperature "correction" has been a source of some difficulty.

4. The notation $U' = \partial_z U$ refers to the ambient shear, and $u' = \partial_z u$ to the shear induced by the orbital wave motion. The distinction is not always so clear.

5. In general, *forward* flow refers to positive $\mathbf{c}\cdot(\mathbf{g} \times \mathrm{curl}\,\mathbf{U})$, where g and U are the vectors of gravity and ambient velocity, respectively.

6. I am indebted to D. Broutman for very considerable improvements of this section, and for the preparation of figure 9.14.

7. The linearized calculations indicated that they are in fact not small.

8. Backward breaking occurs for negative shear; this can be visualized by turning the figure upside down.

9. Frankignoul's (1972) treatment of *finite* amplitude waves [his equations (24) and (28)] lead to precisely the same result.

10. Garrett points out that a lot of laboratory experiments have been sweet-and-sour rather than spicy.

11. It has been suggested that vibration and temperature contamination contributes to the high values from the towed devices; it has also been suggested that the dropped devices have inadequate dynamic range to measure ϵ in the highly active patches where most of the dissipation takes place.

12. A normal-mode formulation is applicable near the boundaries (Watson, Siegmann, and Jacobson, 1977).

13. Frequencies are in $\mathrm{rad\,s^{-1}}$, wavenumbers in $\mathrm{rad\,m^{-1}}$. For comparison with computed spectra we sometimes include (in parenthesis) the values in cycles per hour (cph) and cycles per meter (cpm).

14. We note that $F_e(\omega \gg f) \propto E(\omega, j) \propto \omega^{-2} fE$. There is some evidence that the spectral energy density is independent of latitude (Wunsch and Webb, 1979; Eriksen, 1980), and we should probably replace fE by $N_0 E'$, with $E' = (f_{30°}/N_0)E = 8.8 \times 10^{-7}$ the appropriate f-scaled energy parameter.

15. Desaubies (1973, 1975) explains the observed N-peak in the spectrum and the vertical coherence of vertical displacement.

16. This is related to the "intermittency index" evaluated by Thorpe (1977) from temperature inversions in Loch Ness.

17. "A disorderly state resulting from stress." This descriptive terminology is due to McEwan (1973).